



**HAL**  
open science

# Topology optimization of periodic beam lattices using Cosserat elasticity

Gergely Molnár, Nawfal Blal

► **To cite this version:**

Gergely Molnár, Nawfal Blal. Topology optimization of periodic beam lattices using Cosserat elasticity. Computers & Structures, 2023, 281, pp.107037. 10.1016/j.compstruc.2023.107037 . hal-03831937

**HAL Id: hal-03831937**

**<https://hal.science/hal-03831937v1>**

Submitted on 27 Oct 2022

**HAL** is a multi-disciplinary open access archive for the deposit and dissemination of scientific research documents, whether they are published or not. The documents may come from teaching and research institutions in France or abroad, or from public or private research centers.

L'archive ouverte pluridisciplinaire **HAL**, est destinée au dépôt et à la diffusion de documents scientifiques de niveau recherche, publiés ou non, émanant des établissements d'enseignement et de recherche français ou étrangers, des laboratoires publics ou privés.

# Topology optimization of periodic beam lattices using Cosserat elasticity

Gergely Molnár<sup>a,\*</sup>, Nawfal Blal<sup>a</sup>

<sup>a</sup>*Univ Lyon, CNRS, INSA Lyon, LaMCoS, UMR5259, 69621 Villeurbanne, France*

---

## Abstract

This paper presents a novel method based on the Cosserat theory to optimize the topology of slender metamaterials. First, we compared the optimal topology of discrete Euler-Bernoulli beam lattices with counterparts obtained using the homogenized Cosserat theory. We investigated the effect of material and numerical parameters on the optimization results and the global stiffness. Finally, the paper highlights the importance of second-order models for slender lattice structures through different macroscopic geometries. For the first time, we presented an excellent quantitative agreement between continuum Cosserat and discrete beam results. We demonstrated that the Cosserat theory is necessary and sufficient to optimize slender, lightweight designs with lattice-based microstructures. Furthermore, the results showed that the locally allowed volume fraction was the most critical limiting parameter when maximizing global stiffness. Finally, we found that the reinforced honeycomb lattice is the stiffest microstructure for a given mass among the investigated forms.

*Keywords:* Cosserat elasticity, Topology optimization, Lattice structures, Gradient elasticity, Metamaterial

---

## 1. Introduction

Historically, when creating structures with large spans (*e.g.*, bridges, roofs, or towers), lattice and truss elements were used to reduce the total mass and increase the global stiffness. However, early in history, structural engineers realized that by increasing the space between bent components, the added tensile and compression forces would increase the bending inertia quadratically with the distance (Huygens–Steiner theorem). As a consequence, the additional bending momentum would magnify not only the stiffness but also the global stability of the structures. This way, structures can span considerable distances that are not accessible to solid forms.

A similar phenomenon is seen in nature. A structural hierarchy is found when observing the microstructure of diverse load-bearing components. Examples range from cork [16], through many Diatom species [30], honeycombs [44] and the trabecular bone [35, 50]. In all cases, smaller beam-like elements form an intricate network based on the characteristic loads.

In recent years, with the advancements in additive manufacturing, metamaterials with custom-made microstructures have been prepared [6]. In addition to an increased stiffness, this small-scale procedure makes the load-bearing elements stronger. Moreover, as the material approaches its microscopic length scale, the manufacturing defects' size and effect are reduced. As a result, macroscopically brittle materials might behave in a ductile manner [73, 7] thereby giving rise not only to a lightweight and stiff material but also a resistant one.

Thanks to the advanced manufacturing processes, developing new products with specific optimized properties is possible by modifying their shape or topology. Topology optimization provides a suitable mathematical framework to optimize the material distribution, *i.e.*, the spatial distribution of the material in a design domain. After defining a cost function to be minimized, the sensitivity analysis provides an updating scheme for the design variables. The cost function can be defined for various quantities of interest (compliance, maximal stress, target shape, displacements, etc.). Topology optimization problems can be considered constrained as Partial Differential Equation (PDE) design problems, requiring a combination of optimization solvers and numerical discretization schemes to solve the PDEs physical equations (mainly the finite element method). Two types of optimization solvers can be used: (i) meta-heuristic approaches needing only a back run call of different cost function computations [19] and (ii) gradient-based solvers where the derivative of the cost function is required. Gradient-based topology optimization is usually based on the adjoint state method.

---

\*Corresponding author

*Email address:* gergely.molnar@insa-lyon.fr (Gergely Molnár)

27 The literature cites several approaches for topology optimization. Density-based techniques pioneered by the standard  
28 Solid Isotropic Material with Penalization (SIMP) method [9, 11] have proven their efficiency in structural topology  
29 design for a broad range of applications. SIMP considers density variables defined at each element of the finite element  
30 discretization as the optimized topology’s design parameters (design variables). The main idea is to consider the elastic  
31 behavior at each element designated by a power law introducing a density variable that has a value between 0 (no material)  
32 and 1 (material) and a power law parameter (larger than 1) aiming to penalize intermediate densities. Consequently, when  
33 the penalization parameter is adequately chosen, the spatial material distribution leads to an optimized structure with  
34 only two material types: void regions (elements with no stiffness) and solid regions (elements whose stiffnesses equal the  
35 bulk behavior). Empirically, the penalization parameters are taken to be greater than 3. However, the works of Bendsoe  
36 and Sigmund [10] propose a rigorous methodology for their calibration.

37 One other important issue when using such approaches is the checkerboard pathology. It is due to the apparition  
38 of neighboring elements with alternating void and solid materials. This problem can be addressed with the use of filter  
39 solutions. Usually, one can employ density filters to impose limitations on the density variation by a fixed length scale in  
40 the stiffness distribution. Another option is to introduce sensitivity filtering so that the design sensitivity is maintained in a  
41 fixed neighborhood. Filtering techniques are efficient for limiting mesh-dependency in density-based topology optimization  
42 solvers [12].

43 The other class of topology optimization is based on the level-set function as a parametrization of the design domain  
44 topology [56, 47]. The level-set function represents the boundaries between void and solid phases, and the spatial evolution  
45 of the void-solid interfaces is usually governed by a shape derivative [59] or a topological derivative [29] to find the gradient  
46 direction toward the optimized topology. In recent years, numerous investigations have been proposed for level-set-based  
47 topology optimization approaches [4, 3, 67, 45].

48 Thanks to the recent advent of manufacturing technologies, the design of advanced materials, incorporating small scales  
49 with complex topologies, has become possible. However, simulations for structural optimization describing the finest scales  
50 are computationally expensive. Therefore, multi-scale topology optimization techniques have emerged as a macro-to-micro  
51 optimization technique with noteworthy performances. The optimized structure results from the macro topology design  
52 as the optimized representation of ascribed microstructures (which can be spatially varying). Such two-scale optimization  
53 bridges the underlying scales with less expansive effort while capturing relevant microstructural effects. However, the  
54 optimization process considers the microstructure effect exclusively by its effective (homogenized) behavior. Various  
55 previous studies have investigated the potential macro-micro design optimization [37, 31, 28, 71, 65, 26, 55, 70, 63, 42]],  
56 and most of the corresponding papers are based on scale separation assumptions and periodic homogenization theory.  
57 In order to accelerate multi-scale processes, approaches merging data-driven techniques have recently been developed to  
58 accelerate multi-scale topology optimization solvers [21, 66, 33, 72, 20].

59 The main explorations deal with the framework of the Cauchy theory, and the methods are thus suitable for large-scale  
60 transitions but limited to exhibiting the microstructure size effects. Moreover, such first-order frameworks fail when the  
61 scale separation assumption does not prevail (*e.g.*, when topology cells are kinematically coupled as in some compliant  
62 mechanisms). Enriched kinematic homogenization schemes are needed to efficiently design architected materials and  
63 capture local microstructural effects, mutual interactions, non-localities, or instabilities.

64 One of the first higher-order theories was proposed by the Cosserat brothers [18]. They enriched the simple Cauchy  
65 model with an independent rotation field gradient. This way, the model had three displacement and three rotational  
66 degrees of freedom (in 2D: two displacements DoFs and one rotation DoF). This theory was the first to define couple  
67 stresses and to render the Cauchy stress tensor non-symmetric. Since its first introduction, Toupin [62] formulated the  
68 energy density function using the classic displacement and rotation gradient terms. Finally, Mindlin [43] gave the linearized  
69 mathematical theory, serving as the basis of the variational solution.

70 Since its first introduction, the Cosserat theory has been used in numerous fields such as granular materials [39],  
71 masonry structures [1], composites [34], or even human bone [36, 46]. However, most importantly, it was shown that  
72 Cosserat elasticity efficiently captures the effect of the intrinsic length scale in cellular structures [53]. The constitutive  
73 equations of the model can be written in several forms ranging from a single added constant to Hooke’s law [2] to the  
74 entirely redefined stiffness matrix [69]. However, one of the main disadvantages of the Cosserat theory is that it has too  
75 many material parameters.

76 Bottom-up homogenization methods are usually applied to determine the elastic Cosserat constants of lattice structures.  
77 Two main approaches exist: (i) the micro-scale is represented by an inhomogeneous Cauchy continuum [25, 22, 24, 23], and  
78 (ii) the lattices are modeled with either Euler-Bernoulli [48, 54, 49] or Timoshenko–Ehrenfest beams [40]. The important  
79 difference is that in the latter case, the rotational degrees of freedom are already present at the microscale. On the other  
80 hand, with beam theory, the solid volume fraction cannot be represented. This paper focuses on analytical results obtained

81 using the asymptotic method on Euler-Bernoulli beams [48, 54], and the limitations of the model are discussed.

82 In recent years, various studies have been devoted to obtaining the optimal topology with a characteristic length  
 83 scale by using the Cosserat theory. Most works have focused on fictitious materials with only a few elastic constants.  
 84 Parameter studies have been conducted to investigate the effect of the intrinsic length [27, 52, 41, 5, 38], the fundamental  
 85 eigenfrequencies [13, 60, 61], the Cosserat shear modulus [17], and even 3D non-centrosymmetry [64]. A majority of  
 86 the investigations were based on the use of the SIMP and the level set methods to obtain the results.

87 Among the various models proposed in the literature, second gradient elasticity (such as a Cosserat medium) and  
 88 micromorphic [68, 51] computational homogenization methods seem to be adequate tools to be integrated into topology  
 89 optimization simulations. Indeed, encouraging recent results for bottom-up multiscale modeling of microstructural mate-  
 90 rials with enriched kinematics revive their use in design optimization. However, this topic remains an open research field  
 91 [14].

92 Most studies focusing on the topology optimization of the Cosserat medium use fictitious material parameters, whereas  
 93 papers presenting the optimization of lattice structures calculate only the Cauchy coefficients [66]. A comparative analysis  
 94 using real microstructures and a homogenized second-order continuum has yet to be performed.

95 In the present paper, we present a new method to optimize the topology of slender lattice structures with small local  
 96 volume fractions. We compare the optimal topology of discrete Euler-Bernoulli beam lattices to topologies obtained using  
 97 the Cosserat theory. The local stiffness is calculated based on real geometrical properties, such as the beam height or  
 98 the slenderness. We finally highlight the importance of the enriched model in the optimization of lattice structures and  
 99 present optimal microstructures for a variety of macroscopic mechanical problems.

100 The paper is structured as follows. First, section 2 introduces the basic concept of topology optimization, after which  
 101 section 3 lays out the different mechanical descriptions. Subsequently section 4 discusses the effect of both numerical and  
 102 lattice parameters on the optimal topology. This is followed by a discussion on the optimal microstructure in section 5.  
 103 Finally, section 6 concludes the paper.

## 104 2. Topology optimization

105 Topology optimization is a design method in which the material is distributed inhomogeneously in the design domain  
 106 to maximize a specific property. We chose to use the algorithm published by Sigmund [58] and replaced the arbitrary  
 107 design variable with the height of the beams. Among its advantages, the modified algorithm is easy to implement, robust,  
 108 and converges rapidly. Despite that Bendsøe and Sigmund [10] showed that, for the SIMP method, the cubic penalty  
 109 function is physically permissible, we decided to use the constitutive analytic relations. Based on the Bernoulli beam  
 110 theory, the Cosserat stiffness constants used in this paper were deduced from asymptotic approaches [48, 54]. In addition,  
 111 constraints on the maximum height and volume ratios are discussed in section 3.

112 The overall aim of the topology optimization procedure is to keep the compliance of the model at a minimum by  
 113 minimizing the potential energy as a function of the local design variables:

$$\mathbf{h} = \text{Arg inf}_{\mathbf{h}} \left\{ c(\mathbf{h}) = \frac{1}{2} \mathbf{U}^T \mathbf{K} \mathbf{U} = \frac{1}{2} \sum_{e=1}^N \mathbf{u}_e^T \mathbf{k}_e(h_e) \mathbf{u}_e \right\}. \quad (1)$$

114 This was done by respecting the equilibrium constraint:

$$\mathbf{K} \mathbf{U} = \mathbf{F}, \quad (2)$$

115 and the volume constraint:

$$\frac{V(\mathbf{h})}{V_0} = f, \quad (3)$$

116 with a lower and an upper limit on the design variables (beam heights):

$$0 < \mathbf{h}_{\min} \leq \mathbf{h}_e \leq \mathbf{h}_{\max}. \quad (4)$$

117 In eq. (1),  $c$  is the total potential energy,  $\mathbf{U}$  and  $\mathbf{u}_e$  are the vectors of the global and elementary degrees of freedom  
 118 (translation, rotation),  $\mathbf{K}$  and  $\mathbf{k}_e$  are the global and elementary stiffness matrices,  $N$  is the number of finite elements in  
 119 the design domain, and  $\mathbf{h}$  is the vector containing the elementary design variables ( $h_e$ ). In our case, this is the height of  
 120 the beam cross sections. In this paper, we assume rectangular beam sections with a unitary thickness in the out-of-plane

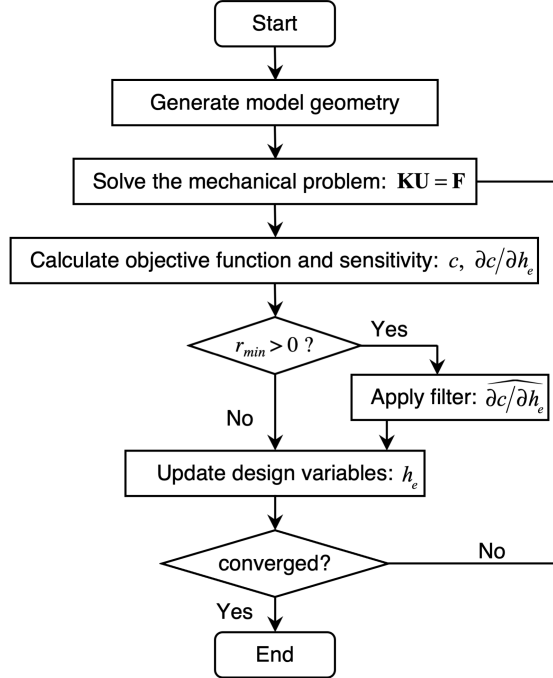


Figure 1: Basic structure of the topology optimization algorithm.

121 ( $z$ ) direction. In the equilibrium equation (2),  $\mathbf{F}$  is the global force vector,  $V$  is the total volume of the model,  $V_0$  is the  
 122 volume of the design domain and  $f$  is called the relative density or prescribed volume fraction.

123 The optimization problem is formulated based on the algorithm proposed by Sigmund [58]. Apart from that work, the  
 124 penalty exponent was replaced by the exact stiffness as a function of the beam height (the design variable); as in lattice  
 125 structures, this variable comes with a physical meaning. The optimality criteria method [8] with a sensitivity filter [57]  
 126 was utilized to update the design variables for a given equilibrium problem.

127 As shown in Fig. 1, we kept the original structure of Ref. [58]. However, we replaced each block with our own features.  
 128 As the paper discusses different mechanical descriptions (Cauchy, Cosserat, Euler-Bernoulli beam) for the same mechanical  
 129 problem, these blocks varied accordingly.

130 First, the finite element model was generated, after which the first equilibrium was obtained. The analytic solutions  
 131 were applied to calculate the stiffness, energy, and sensitivity functions. For the Cosserat medium, the results of refer-  
 132 ences [48] and [54] were utilized. Finally, the filter was applied directly to the array containing the sensitivity functions,  
 133 as initially done by Sigmund [58] where  $r_{min}$  was the effective filter distance. Next, the design variables were updated  
 134 iteratively to satisfy the volume constraint. Finally, the convergence was verified: if the maximum change in the design  
 135 variable was smaller than  $(h_{max} - h_{min})/1000$ , the algorithm was stopped. Otherwise, a new equilibrium was determined  
 136 with the new design variable distribution.

### 137 3. Mechanical description

138 This section briefly summarizes the basic mechanical descriptions used in the paper. All simulations assumed a static  
 139 equilibrium, wherefore, each model was governed by a set of equations describing equilibrium, the kinetic constraints, and  
 140 the material model.

#### 141 3.1. Cauchy continuum

142 In continuum mechanics, probably one of the most frequently used assumptions is proposed by Cauchy [15]. The  
 143 equilibrium of the differential object is depicted in Fig. 2(a) and can be described with the following set of equations:

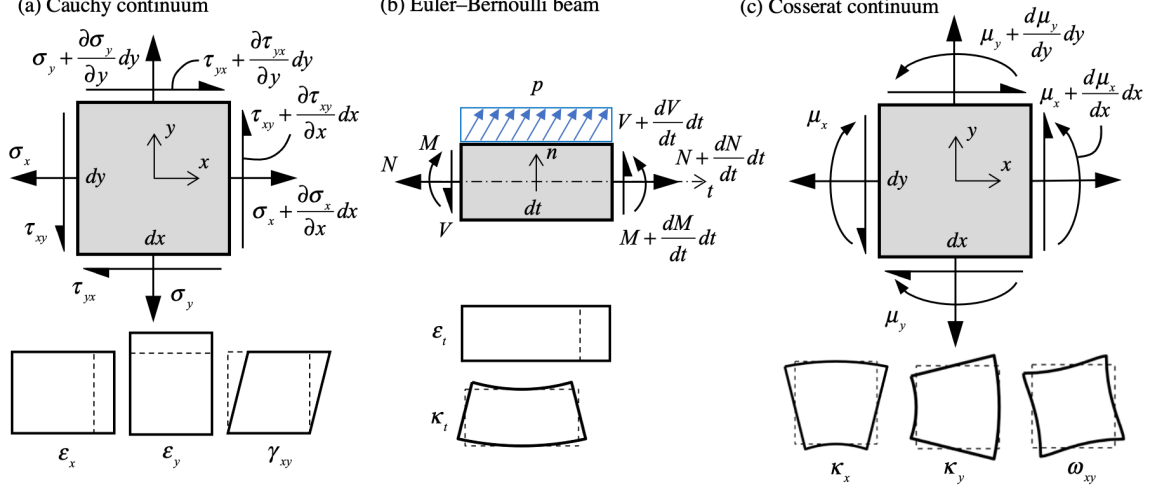


Figure 2: Equilibrium and admissible deformations of the elementary volume of the (a) Cauchy, (b) Euler-Bernoulli beam, and (c) Cosserat theories.

$$\begin{aligned}
 \nabla \boldsymbol{\sigma} + \mathbf{b} &= \mathbf{0} & \text{in } \Omega, \\
 \boldsymbol{\sigma} \cdot \mathbf{n} &= \bar{\mathbf{t}} & \text{on } \Gamma_N, \\
 \mathbf{u} &= \bar{\mathbf{u}} & \text{on } \Gamma_D,
 \end{aligned} \tag{5}$$

144 where  $\boldsymbol{\sigma}$  is the stress tensor, and  $\mathbf{b}$  represents body forces (in our case zero). The second and third rows describe  
 145 respectively Neumann and Dirichlet boundary conditions. The bar symbol represents external forces ( $\bar{\mathbf{t}}$ ), and prescribed  
 146 displacements ( $\bar{\mathbf{u}}$ ).

147 The material is considered to be linear elastic:

$$\boldsymbol{\sigma} = \mathbf{C}\boldsymbol{\varepsilon}, \tag{6}$$

148 where  $\mathbf{C}$  is the stiffness matrix, and  $\boldsymbol{\varepsilon}$  the strain tensor. Due to the local equilibrium ( $\sigma_{xy} = \sigma_{yx} = \tau_{xy}$ ) the Voigt  
 149 notation can be used, thus simplifying the stress tensor to a vector with 3 components in 2D:  $\boldsymbol{\sigma} = [\sigma_x \ \sigma_y \ \tau_{xy}]^T$ .  
 150 Consequently,  $\mathbf{C}$  becomes a  $3 \times 3$  matrix. The strain tensor is also simplified to the three elementary deformations shown  
 151 in Fig.2(a). Assuming small deformations, the displacement-strain relationship can be expressed as:

$$\varepsilon_x = \frac{\partial u_x}{\partial x}, \varepsilon_y = \frac{\partial u_y}{\partial y}, \gamma_{xy} = \frac{\partial u_x}{\partial y} + \frac{\partial u_y}{\partial x}. \tag{7}$$

152 To solve the mechanical problem, the following energy is minimized with respect to the degrees of freedom by following  
 153 the kinematically admissible set given in eq. (5)<sub>3</sub>. In this first case, the displacements are obtained by solving the following  
 154 minimization problem:

$$\mathbf{u} = \text{Arg inf}_{\mathbf{u}} \left\{ \int_{\Omega} \frac{1}{2} \boldsymbol{\varepsilon}^T \mathbf{C} \boldsymbol{\varepsilon} - \mathbf{b} \cdot \mathbf{u} d\Omega - \int_{\Gamma} \bar{\mathbf{t}} \cdot \mathbf{u} d\Gamma \right\}. \tag{8}$$

### 155 3.2. Euler-Bernoulli model

156 To model slender beam structures, the Euler-Bernoulli beam theory provides the most approachable framework. The  
 157 classical beam theory is adapted to describe the behavior of elongated load-bearing elements with one side significantly  
 158 larger than the others. The three primary assumptions that have to be made are that (i) the plane sections remain plane,  
 159 (ii) the plane sections are perpendicular to the neutral axis, and (iii) the deformed beam angles are small. Thus, the  
 160 equilibrium shown in Fig. 2(b) can be described by the following equations:

$$\begin{aligned}\frac{d^2 M}{dt^2} + p_n &= 0, \\ \frac{dN}{dt} + p_t &= 0.\end{aligned}\tag{9}$$

161 Here,  $M$  and  $N$  represent the bending moment and the normal force, and  $p_n$  and  $p_t$  are distributed loads perpendicular  
162 and parallel to the neutral axis. These equations are completed with Neumann and Dirichlet boundary conditions similar  
163 to that of eq. (5)<sub>2,3</sub>. The Euler-Bernoulli beam theory neglects the effect of shear deformation, and as a result, it is  
164 adapted to describe the response of slender beams. The linear elastic response can be obtained by:

$$\begin{aligned}M &= EI\kappa_t, \\ N &= EA\varepsilon_t,\end{aligned}\tag{10}$$

165 where  $\kappa_t$  and  $\varepsilon_t$  are the two types of deformations present beams can be subjected to: (i) curvature/bending and (ii)  
166 elongation/compression.  $E$  is Young's modulus,  $I$  is the bending moment of inertia around axis  $z$ , and  $A$  is the area of  
167 the cross-section.

168 To obtain the relationship between the degrees of freedom and the deformations, the following assumptions are used:

$$\kappa_t = \frac{\partial\phi}{\partial t} = \frac{\partial^2 u_n}{\partial t^2}, \quad \varepsilon_t = \frac{\partial u_t}{\partial t},\tag{11}$$

169 where  $\phi$  is the rotation,  $u_n$  is the perpendicular displacement, and  $u_t$  is the parallel displacement in relation to the  
170 neutral axis.

171 To obtain equilibrium, the following energy functional is minimized by following the kinematically admissible set:

$$(\mathbf{u}, \phi) = \text{Arg inf}_{\mathbf{u}, \phi} \left\{ \int_L \frac{1}{2} (\varepsilon_t^2 EA + \kappa_t^2 EI) dL - \mathbf{p} \cdot \mathbf{u} dL - \bar{\mathbf{t}} \cdot \mathbf{u} - \bar{M} \cdot \phi \right\}.\tag{12}$$

172 The bar symbol represents external forces ( $\bar{\mathbf{t}}$ ), and moments ( $\bar{M}$ ).

### 173 3.3. Cosserat continuum

174 The classical description of continuum mechanics is ill-suited to characterize the response of materials with an inhomogeneous  
175 microstructure, *i.e.*, a characteristic microscopic length scale. However, the mechanical behavior of architected  
176 materials (*e.g.*, lattice structures) is often determined by their specific micro-scale configurations. Therefore, the Cosserat  
177 theory (or micropolar elasticity) incorporates rotational degrees of freedom ( $\phi$ ) into the mechanical description.

178 The Cauchy model is completed with an additional set of equations describing momentum equilibrium as shown in  
179 Fig. 2(c):

$$\begin{aligned}\nabla \boldsymbol{\sigma} + \mathbf{b} &= \mathbf{0} & \text{in } \Omega, \\ \nabla \boldsymbol{\mu} + \boldsymbol{\sigma} \hat{\boldsymbol{\epsilon}} &= \mathbf{0} & \text{in } \Omega, \\ \boldsymbol{\sigma} \cdot \mathbf{n} &= \bar{\mathbf{t}} & \text{on } \Gamma_N, \\ \boldsymbol{\mu} \cdot \mathbf{n} &= \bar{M} & \text{on } \Gamma_N, \\ \mathbf{u} &= \bar{\mathbf{u}} & \text{on } \Gamma_D, \\ \phi &= \bar{\phi} & \text{on } \Gamma_D.\end{aligned}\tag{13}$$

180 In this equation,  $\boldsymbol{\sigma}$  is now a non-symmetric ( $\sigma_{xy} \neq \sigma_{yx}$ ) force-stress tensor,  $\boldsymbol{\mu}$  is the moment or couple-stress tensor,  
181 and  $\hat{\boldsymbol{\epsilon}}$  is the Levi-Civita symbol. The bar symbol represents external forces ( $\bar{\mathbf{t}}$ ), moments ( $\bar{M}$ ), prescribed displacements  
182 ( $\bar{\mathbf{u}}$ ), and rotations ( $\bar{\phi}$ ).

183 The literature [24] recounts various ways to define linear elastic behavior. In this paper, we chose to correlate the  
184 complete stress tensor to the deformation components using the following model:

$$\begin{bmatrix} \sigma_x \\ \sigma_y \\ \tau_{xy} = \frac{\sigma_{xy} + \sigma_{yx}}{2} \\ \vartheta_{xy} = \frac{\sigma_{xy} - \sigma_{yx}}{2} \\ \mu_x \\ \mu_y \end{bmatrix} = \begin{bmatrix} [\mathbf{C}]_{3 \times 3} & \mathbf{0} & \mathbf{0} \\ \mathbf{0} & G_c & \mathbf{0} \\ \mathbf{0} & \mathbf{0} & [\mathbf{D}]_{2 \times 2} \end{bmatrix} \begin{bmatrix} \varepsilon_x \\ \varepsilon_y \\ \gamma_{xy} \\ \omega_{xy} \\ \kappa_x \\ \kappa_y \end{bmatrix}.\tag{14}$$

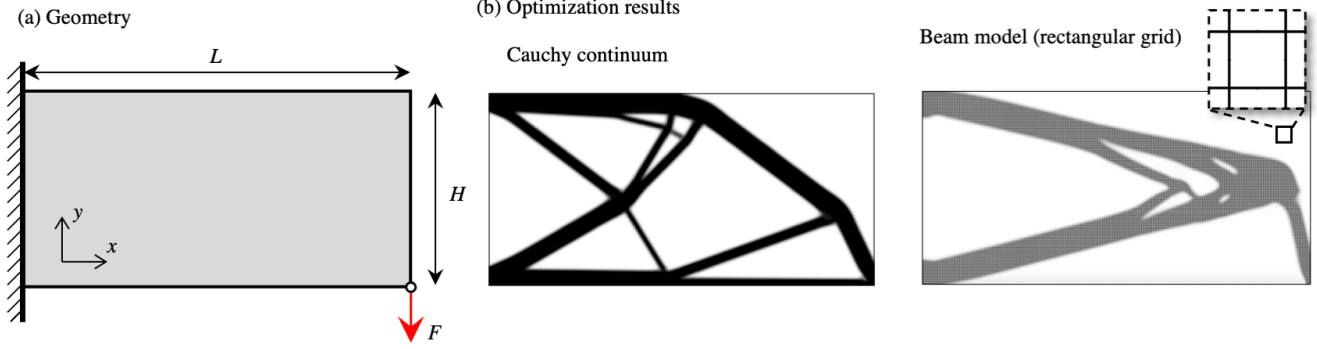


Figure 3: Optimized topology of a cantilever: (a) geometry ( $L = 100$ ,  $H = 50$ ), (b) optimal topology using the Cauchy and the beam model for  $f = 0.12$  ( $r_{\min} = 1$ ).

185 As a result, the first three elements of the stress vector correspond to the Cauchy stress components, the fourth element  
 186 provides the difference between  $\sigma_{xy}$  and  $\sigma_{yx}$ , finally, the last components are the couple stresses.

187 The corresponding deformations are depicted in Fig. 2(c), with the missing kinematic constraints described by the  
 188 following:

$$\omega_{xy} = \frac{\partial u_x}{\partial y} - \frac{\partial u_y}{\partial x} - 2\phi, \quad \kappa_x = \frac{\partial \phi_x}{\partial x}, \quad \kappa_y = \frac{\partial \phi_y}{\partial y}. \quad (15)$$

189 The equilibrium is then obtained by minimizing the following functional equations:

$$(\mathbf{u}, \phi) = \text{Arg inf}_{\mathbf{u}, \phi} \left\{ \int_{\Omega} \frac{1}{2} [\boldsymbol{\varepsilon}^T \mathbf{C} \boldsymbol{\varepsilon} + \omega_{xy}^2 G_c + \boldsymbol{\kappa}^T \mathbf{D} \boldsymbol{\kappa}] - \mathbf{b} \cdot \mathbf{u} d\Omega - \int_{\Gamma} \bar{\mathbf{t}} \cdot \mathbf{u} + \bar{m} \cdot \phi d\Gamma \right\}. \quad (16)$$

190 By incorporating rotational degrees of freedom into the continuum description, the Cosserat theory proposes an  
 191 analogous description to the discrete beam model with a significantly lower computational cost.

#### 192 4. Numerical examples

193 Fig. 3(a) depicts the geometry of the optimization problem. In this section, a cantilever geometry of length ( $L$ ) 100  
 194 and height ( $H$ ) 50 was chosen. The concentrated force ( $F$ ) applied at the end was  $10^{-3}$  unless otherwise specified. This  
 195 paper presents the model and the results in dimensionless quantities. Young's modulus was set to 1. Both translational  
 196 and rotational degrees of freedom were constrained on the nodes on the left side.

197 For a beam structure, the volume constraint defined in eq. (3) can be expressed by summing up all the individual  
 198 elements and dividing the sum by the overall area of the design domain:

$$f = \frac{V(\mathbf{h})}{V_0} = \frac{\sum_{e=1}^N h_e l_e}{LH}, \quad (17)$$

199 where  $V_0$  is the total volume of the design domain,  $l_e$  represents the individual length of the beams, and  $h_e$  is their  
 200 height. There are  $N$  beams in the structure. In this case,  $h_e$ , The design variable has a geometrical significance wherefore  
 201 its bounds can be defined as:

$$0 < h_{\min} \leq h_e \leq h_{\max}, \quad (18)$$

202 with  $h_{\min}$  as a lower bound responsible for numerical stability ( $h_{\min} = h_{\max}/5000$ ), and  $h_{\max}$  as an upper bound:

$$h_{\max} \leq \frac{V_0}{\sum_{i=1}^N l_i}. \quad (19)$$



Lattice type	$l_x$	$l_y$	$\sum l_e$	$V_{\text{RVE}}$	$h(f_{\text{RVE}})$	$f_{\text{RVE}}(h)$	$f_{\text{RVE}}(l_e/h = 5)$
Rectangular	$l_m$	$l_m$	$2l_m$	$l_m^2$	$\frac{l_m f_{\text{RVE}}}{2}$	$\frac{2h}{l_m}$	0.4
Honeycomb	$\sqrt{3}l_m$	$3l_m$	$6l_m$	$3\sqrt{3}l_m^2$	$\frac{\sqrt{3}}{2}l_m f_{\text{RVE}}$	$\frac{2h}{\sqrt{3}l_m}$	$\frac{2}{5\sqrt{3}} = 0.23$
Reinforced honeycomb	$\sqrt{3}l_m$	$3l_m$	$l_m(6 + 6\sqrt{3})$	$3\sqrt{3}l_m^2$	$\frac{\sqrt{3}l_m f_{\text{RVE}}}{2+2\sqrt{3}}$	$\frac{h}{l_m} \frac{2+2\sqrt{3}}{\sqrt{3}}$	$\frac{2+2\sqrt{3}}{5\sqrt{3}} = 0.63$

Table 1: Lattice geometries and correlation between volume ratio and beam height.

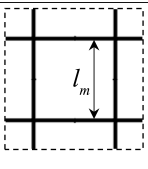
Lattice type	$C_{11}, C_{22}$	$C_{12}, C_{21}$	$C_{33}$	$G_c$	$D_{11}, D_{22}$
 Rectangular	$\frac{ht}{l_m} E$	0	$\frac{th^3}{2l_m^3} E$	$\frac{th^3}{2l_m^3} E$	$\frac{th^3}{12l_m} E$

Table 2: Cosserat constants for the rectangular beam lattice.

The characteristic quantities, upper bounds, and the correlation between local volume fraction and beam height are summarized in Table 1.

When using  $h_{\text{max}}$ , the RVE should be considered solid ( $f_{\text{RVE}} = 1$ ). This limit is unsuitable for beam theory, and consequently, in the following examples,  $h_{\text{max}}$  is set to  $l_e/5$ , at which value the Euler-Bernoulli beam theory still gives a fairly precise outcome (the difference to the Timoshenko–Ehrenfest theory is 3.06%).

Part (b) of Fig. 3 shows the optimization results of a rectangular lattice modeled using the Cauchy continuum (with SIMP) and Euler-Bernoulli beams. When employing the Cauchy description, the design variable was penalized using a cubic function, and the maximum value of the design variable was limited to 0.4, which corresponds to the volume ratio of the rectangular grid RVE when  $h_e = l_m/5$ . It can be clearly seen that Cauchy’s description with the SIMP technique is unable to correctly determine the optimal topology.

In the present paper, we discuss three microstructures: square, hexagonal, and reinforced honeycomb lattices. The reason for this is that the analytic Cosserat stiffness components for these structures are available in the literature [48, 54]. Tables 2 and 3 summarize each constant of the matrices  $\mathbf{C}$ ,  $\mathbf{D}$  and the component  $G_c$ . The remaining components of the matrices were zero.

The aim of section 4 is to prove that the Cosserat medium is necessary and sufficient to optimize the topology of light and slender beam lattices. Therefore, each material and numerical parameter was tested using the Euler-Bernoulli beam and the Cosserat theory, after which the optimal topology and the final displacement ( $u_y^F$ ) measured at the concentrated force  $F$  were compared. It should be noted, that the objective function (potential energy) was equal to  $c = Fu_y^F/2$ , and

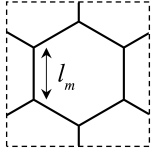
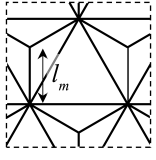
Lattice type	$K_s$	$G_s$	$G_c$	$D_{11}, D_{22}$
 Honeycomb	$\frac{\sqrt{3}}{6} \frac{Eth}{l_m}$	$\frac{Eth^3}{\sqrt{3}l_m(l_m^2+h^2)}$	$\frac{Eth^3}{2\sqrt{3}l_m^3}$	$\frac{Eth^3}{12\sqrt{3}l_m}$
 Reinforced honeycomb	$\frac{3+\sqrt{3}}{6} \frac{Eth}{l_m}$	$\frac{t^2h^6 + \frac{4}{3}(\sqrt{3}+1)t^2h^4l_m^2 + l_m^4t^4h^4}{4l_m^3(l_m^2th+th^3)} E$	$\frac{3+\sqrt{3}}{6\sqrt{3}} \frac{Eth^3}{l_m^3}$	$\frac{1+\sqrt{3}}{12\sqrt{3}} \frac{Eth^3}{l_m}$

Table 3: Cosserat constants for honeycomb and reinforced honeycomb beam lattices.  $C_{11} = C_{22} = K_s + G_s$ ,  $C_{12} = C_{21} = K_s - G_s$ ,  $C_{33} = G_s$ .

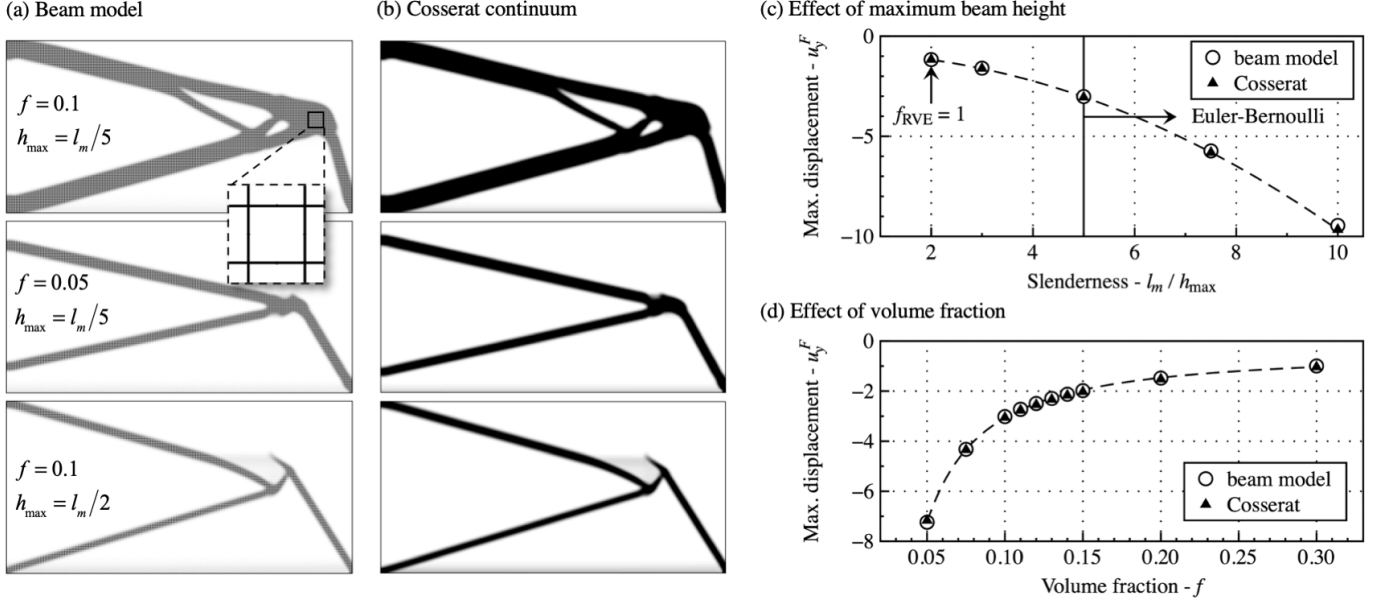


Figure 4: Topology and deflection results on a rectangular grid as a function of local and global volume fractions.

221 the potential energy was thus not an independent measure of optimality.

#### 222 4.1. Square lattice

223 The homogenized stiffness of a rectangular grid lattice is orthotropic. The two principal orientations are parallel to the  
 224 two main beam directions. Due to the lack of normal interaction,  $C_{12} = 0$ , which means that extension in one direction  
 225 causes no contraction in the other. This property signifies that the homogenized material's Poisson's ratio is zero ( $\nu = 0$ ).  
 226 The rectangular beam lattice was used to demonstrate the effect of the volume fractions on the optimal topology. We  
 227 distinguish between local  $f_{RVE}$  and global  $f$  values, where  $f_{RVE}$  represents the allowed maximum local volume fraction,  
 228 while  $f$  is the global volume fraction defined in eq. (17). These two quantities are independent, with  $f \leq f_{RVE}$ , and  $f_{RVE}$   
 229 is mostly controlled by prescribing a lower beam height in the model based on the correlation shown in Table 1. Due to  
 230 the difference in local geometry, various lattice structures have different  $f_{RVE}$  for the same  $l_e/h_e$  ratio.

231 The beam model was constructed from  $300 \times 150$  RVEs. The beam segments were unified, which resulted in 90 450  
 232 beam finite elements with  $l_m = 1/3$ . The load was applied on a node situated on the bottom line furthest to the right.  
 233 The Cosserat model was divided into  $300 \times 150$  4-node quadrilateral elements. We used 45000 elements to capture similar  
 234 topology details as in the beam model. The advantage of the Cosserat model is that  $l_m$  reduces to a material parameter,  
 235 and the element size does not affect it. The material and the boundary conditions can be found in the main part of  
 236 Section 4. A filter of  $r_{\min} = 1$  was used in both cases.

237 The first two rows of Fig. 4(a) and (b) show the optimal topology for two global volume fractions obtained using a  
 238 beam model (left) and the Cosserat continuum (right). The third row portrays the change if thicker beams are allowed.  
 239 The results displayed in the two columns are almost identical. However, they differed significantly from the outcome  
 240 obtained using the Cauchy continuum and the SIMP technique shown in Fig. 3(b).

241 Similar to the topologies, the displacement results were also in good correspondence. Fig. 4(c) shows the effect of the  
 242 local slenderness. The maximum difference between the deflection values was 2.16%, which was within the precision of  
 243 the built models. Furthermore, we observed a tendency to favor thicker beams. When  $f_{RVE}$  increased, the maximum  
 244 deflection decreased. Without a global stability analysis, the optimal topology favors thinner elements with higher local  
 245 volume fractions. When  $h_{\max}$  was reduced, the size of the global elements grew, raising the moment of inertia but lowering  
 246 the leverage—resulting in a less rigid structure. This effect was demonstrated but not discussed by Watts [66], where the  
 247 optimal topology was fairly independent of the chosen structure, and local maxima gave mostly solid parts (with  $f_{RVE} = 1$ ).  
 248 Of course, this solution defeats the purpose of creating an architected material.

249 Finally, Fig. 4(d) presents a plot of the deflection results as a function of the global volume fraction with  $h_{\max} = l_m/5$   
 250 ( $f_{RVE} = 0.4$ ). The results were fitted perfectly using a hyperbolic function. Moreover, the maximum difference was 3.8%,

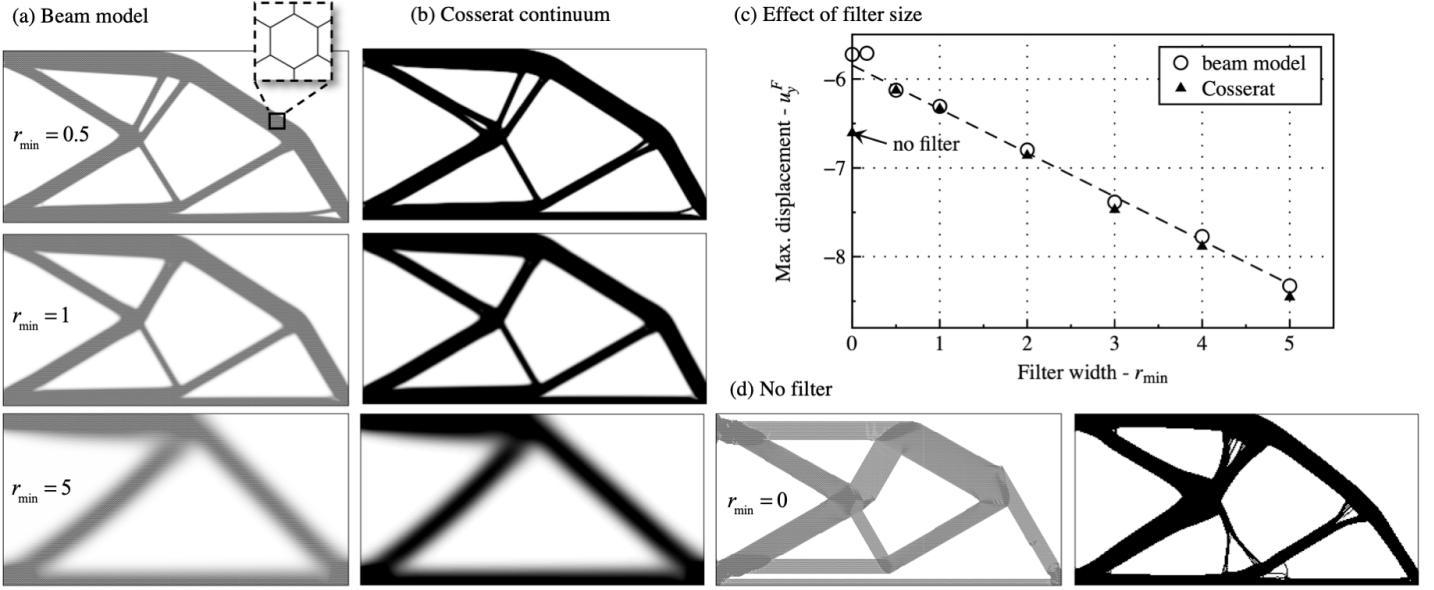


Figure 5: Topology and deflection results on a honeycomb structure as a function of the filter width.

251 which demonstrated how well the Cosserat theory reproduced the mechanical response of these periodic beam structures.

#### 252 4.2. Honeycomb lattice

253 In contrast, the homogenization of honeycomb lattices gives an isotropic response with a Poisson's ratio depending on  
 254 the slenderness varying between 0.3-0.5 (for  $l_e/h_e = 5$ , it is 0.46). Therefore, as shown in Fig. 5, the optimal topologies  
 255 are much closer to the results produced by SIMP. This section thus describes the use of the honeycomb structure to  
 256 demonstrate the effect of the filter width ( $r_{\min}$ ) on the topology and the maximum deflection at the concentrated force  
 257 as a measure of optimality.

258 The beam model was constructed from  $300 \times 87$  RVEs. The beam segments were unified, which resulted in 156 387  
 259 beam finite elements with  $l_m = 0.192$ . The load was applied on a node situated on the bottom line furthest to the right.  
 260 The Cosserat model was divided into  $300 \times 150$  4-node quadrilateral elements (45000 elements), similarly to the rectangular  
 261 case. The material and the boundary conditions can be found in the main part of Section 4. The filter width was varied  
 262 through the analysis.

263 Fig. 5(a) and (b) show the results obtained using Euler-Bernoulli beams and the Cosserat continuum, respectively. An  
 264 agreement was observed, highlighting the Cosserat theory's versatile potential. When the filtering was switched off, the  
 265 two theories started to deviate, as shown in Fig. 5(d). However, it is our opinion that these results bear little practical  
 266 importance.

267 Finally, we plotted the maximum deflection in Fig. 5(c). Introducing the filter reduced the optimality and the overall  
 268 stiffness of the structure. By increasing the filter width, the displacement increased linearly. However, when  $r_{\min}$   
 269 was smaller than the shortest distance between the beam elements, the filter could no longer complete its task, and the results  
 270 started to fluctuate. Until that point, the maximum difference between the two methods was 1.51%.

#### 271 4.3. Reinforced honeycomb lattice

272 Our third example focuses on the effect of the characteristic micro length scale on the reinforced honeycomb network.  
 273 In this case, the classic hexagonal structure was fortified with a triangular grid. While the hexagonal structure was mostly  
 274 a bending-dominated lattice, triangular cells provided normal rigidity. The homogenized Cauchy stiffness was isotropic  
 275 with a Poisson's ratio varying between 0.3-0.34 (for  $l_e/h_e = 5$ , it is 0.325).

276 Different beam structures were created to test the effect of the micro-length. However, only whole RVEs were used  
 277 to create the beam models. Due to the irrational size of the RVE, not many configurations had precisely the same size.  
 278 Therefore, the following sample sizes were considered:  $142 \times 41$ ,  $239 \times 69$ ,  $284 \times 82$ ,  $336$  and  $426 \times 123$ , which corresponded  
 279 to  $l_m = 0.4$ ,  $0.24$ ,  $0.2$ ,  $0.17$  and  $0.14$ , respectively.

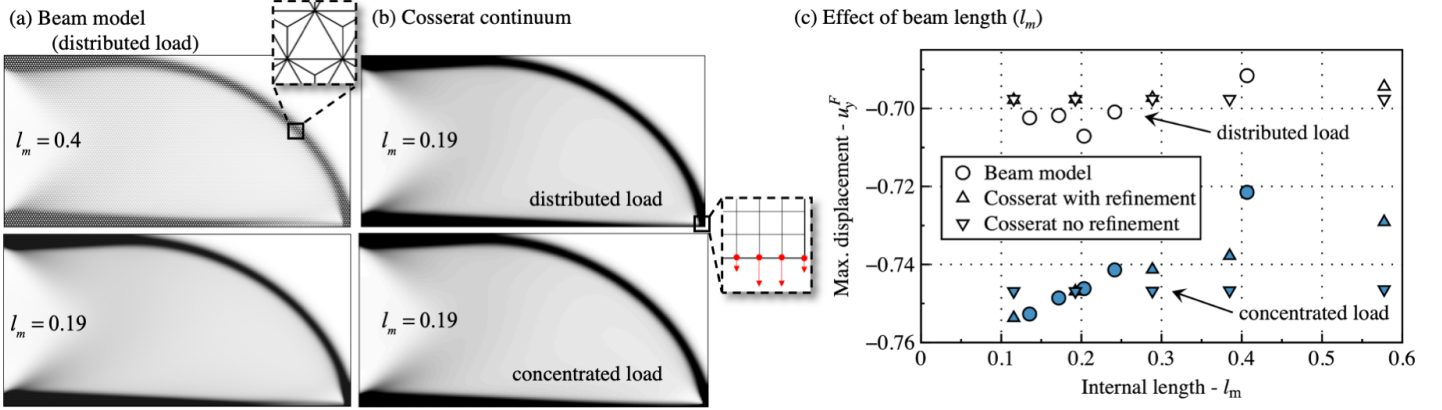


Figure 6: Topology and deflection results on a reinforced honeycomb structure as a function of  $l_m$ . The results for the concentrated force are shown with solid symbols, whereas for the empty ones, the load was distributed on a unit length.

280 The advantage of the Cosserat model is that there is no need to change the mesh for a different  $l_m$  value, as it is only  
 281 a material parameter. However, both models were tested with a mesh following the change of  $l_m$  and one independent  
 282 constant of  $300 \times 150$  elements.

283 The finite element mesh was generated from 4 node quadrilateral elements. The material and the Dirichlet boundary  
 284 conditions can be found in the main part of Section 4. A filter of  $r_{\min} = 1$  was used in both cases.

285 After initial testing, the results showed that the concentrated force and the changing mesh had more significant effects  
 286 on the deflection than  $l_m$ . Therefore, a model was developed to distribute the loading on a unit length. Practically, the  
 287 force was divided and applied on the beam and the continuum model as shown in Fig. 6.

288 Fig. 6(a) and (b) show that neither  $l_m$  nor the Neumann boundary affected the optimal topology. Both the beam and  
 289 Cosserat models gave a solid-like outer shell (with  $f_{\text{RVE}}$ ) and a less filled interior. Fig. 6(c) displays the deflection results  
 290 as a function of  $l_m$ . Its effect was found to be much smaller than the increased deflection originating from the singularity.  
 291 When the load was distributed, a small increase in rigidity was observed in favor of larger motifs.

## 292 5. Discussion

293 In Section 4 we demonstrated that the Cosserat description was sufficient not only qualitatively but also quantitatively  
 294 to describe the mechanical behavior of beam lattice structures. Moreover, the response as well as the optimal topologies  
 295 was found to be in agreement.

296 Here, we take a step back to understand the critical components of the Cosserat description, ultimately investigating  
 297 different structures (design domains) with varying  $L/H$  ratios to identify an "ideal" microstructure.

298 Fig. 7 shows the optimization problem introduced in Section 4. The elementary grid is a rectangular lattice with  
 299  $300 \times 150$  RVEs, and the global volume fraction was set to  $f = 0.12$  with an  $r_{\min} = 1$  filter width. The results were  
 300 compared with those of the beam model shown Fig. 3(b).

301 Fig. 7(a) presents, the optimal topology using the SIMP method with a  $\nu = 0$  material and a cubic penalty. In this  
 302 first case, no limit was applied to the local volume ratio ( $f_{\text{RVE}} = 1$ ), and as a result, the final topology differed significantly  
 303 from the results obtained as compared to the beam lattice. Furthermore, the deflection was much smaller because of the  
 304 higher local volume ratio. As a result, the SIMP method with an isotropic material was inadequate to model slender  
 305 lattice structures. In part (b) the maximum stiffness was calculated with  $f_{\text{RVE}} = 0.4$  based on Tables 1 and 2. To scale  
 306 between empty and solid states, a cubic penalty was applied. This modification was the first step when the form started  
 307 to resemble the results obtained with the beam model. The global form was recovered, however, the details remained  
 308 dissimilar. Part (c) portrays the results when the penalty was omitted, and the stiffness was calculated based on 2. The  
 309 details started to emerge, however, the deflection values overestimated the beam results ( $u_y^F = 2.5$ ) by 7.2%. Finally,  
 310 part (d) presents the optimal topology obtained using the Cosserat theory. The details were fully recovered with a 1.2%  
 311 difference in the deflation value.

312 The introduction of the rotational degree of freedom and the Cosserat theory clearly helped recover the finer details  
 313 and the precise mechanical response of the underlying beam structures. Compared to the classical continuum, the finite

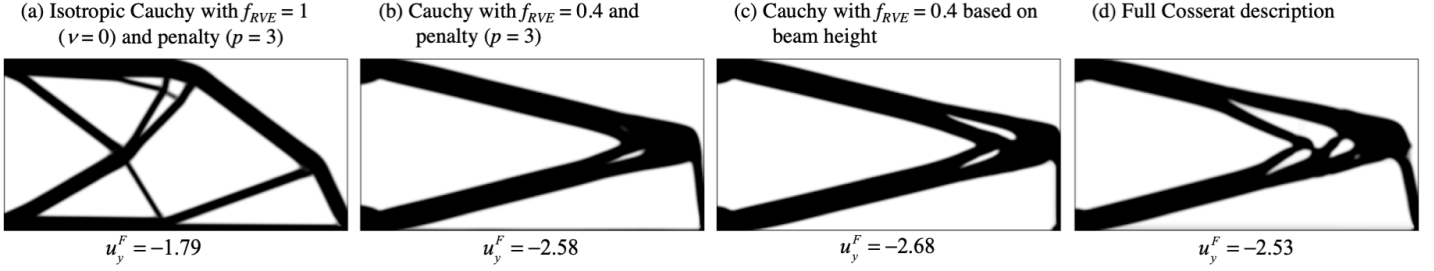


Figure 7: Different approximations of the rectangular grid with the global volume ratio of  $f = 0.12$ : (a) isotropic Cauchy model with a maximum of  $f_{RVE} = 1$  and a cubic penalty; (b) Cauchy model with a maximum of  $f_{RVE} = 0.4$  and a cubic penalty; (c) Cauchy model with a maximum of  $f_{RVE} = 0.4$  based on the beam heights; (d) full Cosserat description. The rigidity was calculated based on Tables 2 and 3. The maximum displacement for the reference beam model at the concentrated load was  $u_y^F = -2.50$  (see topology result in Fig. 3).

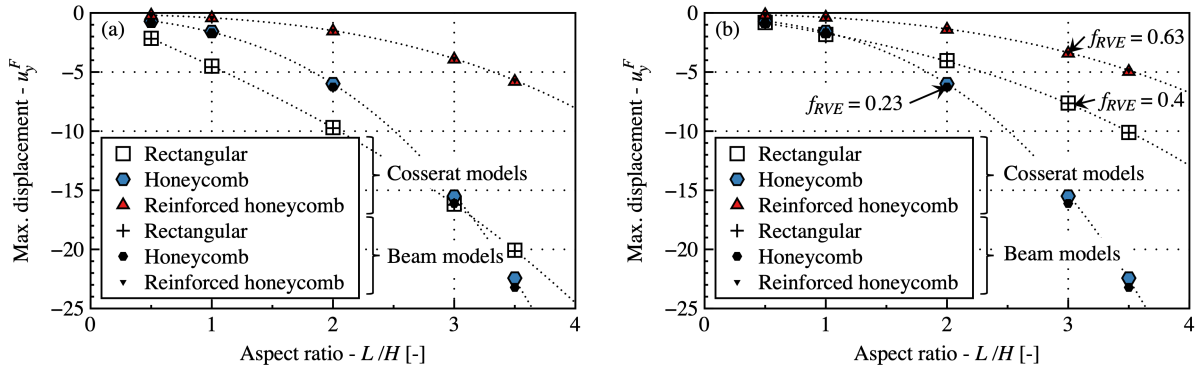


Figure 8: Maximum displacement as a function of the design space's aspect ratio for a global volume ratio of  $f = 0.075$  and  $l_m = 1/3$ : (a) with  $f_{RVE} = 0.23$  for all lattice geometries; (b) with their maximum volume ratios by respecting  $l_e/h_e \geq 5$ .

314 element implementation of the theory was not much more complicated. The only difficulty lies in determining the Cosserat  
 315 constants for arbitrary beam structures. However, this can be done using various homogenization methods [25, 32, 40].  
 316 The Cosserat optimization code used in this paper is included in Supplementary Materials.

317 The aspect ratio of the design space was varied to compare the three lattice structures. We were interested in  
 318 determining whether an optimal microstructure could be found as a function of the geometry. According to Fig. 4(c),  
 319 the locally allowed maximum volume fraction had a significant effect on the deflection results. Therefore, in Fig. 8(a) we  
 320 first compared results using the same local filling ratio,  $f_{RVE} = 0.23$ . Interestingly, there was a competition between the  
 321 honeycomb and the rectangular grid. However, the reinforced honeycomb was consistently more rigid. When the local  
 322 volume fraction of the rectangular grid was increased to 0.4, it became superior to the honeycomb, even in the initial  
 323 interval. The results obtained using the Cosserat theory repeatedly corresponded well to the beam models. It could thus  
 324 be stated that, depending on the design problem, the optimal RVE can be appropriately chosen using Cosserat elasticity.

## 325 6. Conclusion

326 This paper presents a topology optimization algorithm based on the Cosserat theory. The continuum results were  
 327 compared and verified using Euler-Bernoulli beam models, and the stiffness of the enriched medium was determined from  
 328 analytic calculations.

329 We observed an excellent quantitative correspondence between continuum Cosserat and discrete beam results. We  
 330 showed that the Cosserat theory was necessary and sufficient to optimize slender, lightweight designs with beam mi-  
 331 crostructures and that the maximum local volume ratio (thus the maximum beam height) significantly affected the  
 332 optimal deflection values. The effect of the filter width and the local length scale were also tested.

333 The addition of the rotational degree of freedom allowed us to capture the equivalent behavior of the beam theory.  
 334 The advantage of the Cosserat model is that  $l_m$  reduces to a material parameter wherefore, the element size does not

335 affect the microstructure. Consequently, the calculations can be significantly accelerated compared to beam models.

336 While the finite element implementation of the Cosserat theory is relatively simple, the stiffness components are avail-  
337 able analytically only for a few periodic microstructures. Consequently, developing and publishing a universal homoge-  
338 nization algorithm is crucial in order to establish a database with various lattice structures used in practice. Furthermore,  
339 the algorithm should be employed to optimize the beam heights and, for example, the microscopic length scale.

## 340 References

- 341 [1] Addessi, D., Sacco, E., Paolone, A., 2010. Cosserat model for periodic masonry deduced by nonlinear homogenization.  
342 *European Journal of Mechanics - A/Solids* 29, 724–737. doi:10.1016/j.euromechsol.2010.03.001.
- 343 [2] Aifantis, E.C., 1984. On the microstructural origin of certain inelastic models. *Journal of Engineering Materials and*  
344 *Technology* 106, 326–330. doi:10.1115/1.3225725.
- 345 [3] Allaire, G., De Gournay, F., Jouve, F., Toader, A.M., 2005. Structural optimization using topological and shape  
346 sensitivity via a level set method. *Control and cybernetics* 34, 59.
- 347 [4] Allaire, G., Jouve, F., Toader, A.M., 2004. Structural optimization using sensitivity analysis and a level-set method.  
348 *Journal of computational physics* 194, 363–393. doi:10.1016/j.jcp.2003.09.032.
- 349 [5] Arimitsu, Y., Karasu, K., Wu, Z., Sogabe, Y., 2011. Optimal topologies in structural design of micropolar materials.  
350 *Procedia Engineering* 10, 1633–1638. doi:10.1016/j.proeng.2011.04.273.
- 351 [6] Askari, M., Hutchins, D.A., Thomas, P.J., Astolfi, L., Watson, R.L., Abdi, M., Ricci, M., Laureti, S., Nie, L., Freear,  
352 S., Wildman, R., Tuck, C., Clarke, M., Woods, E., Clare, A.T., 2020. Additive manufacturing of metamaterials: A  
353 review. *Additive Manufacturing* 36, 101562. doi:10.1016/j.addma.2020.101562.
- 354 [7] Bauer, J., Schroer, A., Schwaiger, R., Kraft, O., 2016. Approaching theoretical strength in glassy carbon nanolattices.  
355 *Nature materials* 15, 438–443. doi:10.1038/nmat4561.
- 356 [8] Bendsøe, M.P., 1995. Optimization of structural topology, shape, and material. volume 414. Springer. doi:10.1007/978-  
357 3-662-03115-5.
- 358 [9] Bendsøe, M.P., Kikuchi, N., 1988. Generating optimal topologies in structural design using a homogenization method.  
359 *Computer methods in applied mechanics and engineering* 71, 197–224. doi:10.1016/0045-7825(88)90086-2.
- 360 [10] Bendsøe, M.P., Sigmund, O., 1999. Material interpolation schemes in topology optimization. *Archive of applied*  
361 *mechanics* 69, 635–654. doi:10.1007/s004190050248.
- 362 [11] Bendsøe, M.P., Sigmund, O., 2003. *Topology Optimization: Theory, Methods and Applications*. Springer.  
363 doi:10.1007/978-3-662-05086-6.
- 364 [12] Bourdin, B., 2001. Filters in topology optimization. *International Journal for Numerical Methods in Engineering* 50,  
365 2143–2158. doi:10.1002/nme.116.
- 366 [13] Bruggi, M., Taliercio, A., 2012. Maximization of the fundamental eigenfrequency of micropolar solids through topology  
367 optimization. *Structural and Multidisciplinary Optimization* 46, 549–560. doi:10.1007/s00158-012-0779-3.
- 368 [14] Calisti, V., Lebé, A., Novotny, A., Sokolowski, J., 2021. Sensitivity of the second order homogenized elasticity tensor  
369 to topological microstructural change. *Journal of Elasticity* 144, 141–167. doi:10.1007/s10659-021-09836-6.
- 370 [15] Cauchy, A.L., 1823. Recherches sur l'équilibre et le mouvement intérieur des corps solides ou fluides, élastiques ou  
371 non élastiques. *Bulletin de la Société Philomatique* , 9–13. doi:10.1017/CBO9780511702518.038.
- 372 [16] Chen, B., Yuan, Q., Luo, J., Fan, J.H., 2010. Fibre reinforced cellular microstructure of cork wood. *Plastics, Rubber*  
373 *and Composites* 39, 86–90. doi:10.1179/174328910X12608851832650.
- 374 [17] Chen, L., Wan, J., Chu, X., Liu, H., 2021. Parameterized level set method for structural topology optimization based  
375 on the cosserat elasticity. *Acta Mechanica Sinica* 37, 620–630. doi:10.1007/s10409-020-01045-z.

- 376 [18] Cosserat, E., Cosserat, F., 1909. Théorie des corps déformables. Librairie Scientifique A. Hermann et Fils.  
377 doi:10.1038/081067a0.
- 378 [19] Di Cesare, N., Domaszewski, M., 2019. A new hybrid topology optimization method based on i-pr-pso and eso. appli-  
379 cation to continuum structural mechanics. *Computers Structures* 212, 311–326. doi:10.1016/j.compstruc.2018.11.006.
- 380 [20] Djourachkovitch, T., Blal, N., Hamila, N., Gravouil, A., 2021. Multiscale topology optimization of 3d struc-  
381 tures: A micro-architected materials database assisted strategy. *Computers and Structures* 255, 106574.  
382 doi:10.1016/j.compstruc.2021.106574.
- 383 [21] Ferrer, A., Cante, J.C., Hernández, J., Oliver, J., 2018. Two-scale topology optimization in computational ma-  
384 terial design: An integrated approach. *International journal for numerical methods in engineering* 114, 232–254.  
385 doi:10.1002/nme.5742.
- 386 [22] Forest, S., 1998. Mechanics of generalized continua: construction by homogenization. *Le Journal de Physique IV* 8,  
387 39–48. doi:10.1051/jp4:1998405.
- 388 [23] Forest, S., 2002. Homogenization methods and mechanics of generalized continua—Part 2. Theoretical and applied  
389 mechanics , 113–144doi:10.2298/TAM0229113F.
- 390 [24] Forest, S., Pradel, F., Sab, K., 2001. Asymptotic analysis of heterogeneous cosserat media. *International Journal of*  
391 *Solids and Structures* 38, 4585–4608. doi:10.1016/S0020-7683(00)00295-X.
- 392 [25] Forest, S., Sab, K., 1998. Cosserat overall modeling of heterogeneous materials. *Mechanics research communications*  
393 25, 449–454. doi:10.1016/S0093-6413(98)00059-7.
- 394 [26] Gaynor, A.T., Meisel, N.A., Williams, C.B., Guest, J.K., 2014. Multiple-material topology optimization of compliant  
395 mechanisms created via polyjet three-dimensional printing. *Journal of Manufacturing Science and Engineering* 136.  
396 doi:10.1115/1.4028439.
- 397 [27] Gei, M., Rovati, M., Veber, D., 2006. Effect of internal length scale on optimal topologies for cosserat continua,  
398 in: Bendsøe, M.P., Olhoff, N., Sigmund, O. (Eds.), *IUTAM Symposium on Topological Design Optimization of*  
399 *Structures, Machines and Materials*, Springer Netherlands. pp. 157–166. doi:10.1007/1-4020-4752-5\_16.
- 400 [28] Groen, J.P., Sigmund, O., 2018. Homogenization-based topology optimization for high-resolution manufacturable  
401 microstructures. *International Journal for Numerical Methods in Engineering* 113, 1148–1163. doi:10.1002/nme.5575.
- 402 [29] Jackowska-Strumillo, L., Sokolowski, J., Zochowski, A., 1999. The topological derivative method in shape optimiza-  
403 tion, in: *Proceedings of the 38th IEEE Conference on Decision and Control (Cat. No.99CH36304)*, pp. 674–679 vol.1.  
404 doi:10.1109/CDC.1999.832864.
- 405 [30] Jang, D., Meza, L.R., Greer, F., Greer, J.R., 2013. Fabrication and deformation of three-dimensional hollow ceramic  
406 nanostructures. *Nature materials* 12, 893–898. doi:10.1038/nmat3738.
- 407 [31] Kato, J., Yachi, D., Kyoya, T., Terada, K., 2018. Micro-macro concurrent topology optimization for nonlinear solids  
408 with a decoupling multiscale analysis. *International Journal for Numerical Methods in Engineering* 113, 1189–1213.  
409 doi:10.1002/nme.5571.
- 410 [32] Kouznetsova, V., Geers, M.G.D., Brekelmans, W.A.M., 2002. Multi-scale constitutive modelling of heterogeneous ma-  
411 terials with a gradient-enhanced computational homogenization scheme. *International journal for numerical methods*  
412 *in engineering* 54, 1235–1260. doi:10.1002/nme.541.
- 413 [33] Kumar, S., Tan, S., Zheng, L., Kochmann, D., 2020. Inverse-designed spinodoid metamaterials. *npj Computational*  
414 *Materials* 6, 73. doi:10.1038/s41524-020-0341-6.
- 415 [34] Lakes, R., 1991. Experimental Micro Mechanics Methods for Conventional and Negative Poisson’s Ratio Cellular  
416 Solids as Cosserat Continua. *Journal of Engineering Materials and Technology* 113, 148–155. doi:10.1115/1.2903371.
- 417 [35] Lakes, R., 1993. Materials with structural hierarchy. *Nature* 361, 511–515. doi:10.1038/361511a0.
- 418 [36] Lakes, R., Saha, S., 1979. Cement line motion in bone. *Science* 204, 501–503. doi:10.1126/science.432653.

- 419 [37] Li, H., Luo, Z., Gao, L., Qin, Q., 2018. Topology optimization for concurrent design of structures with multi-  
420 patch microstructures by level sets. *Computer Methods in Applied Mechanics and Engineering* 331, 536–561.  
421 doi:10.1016/j.cma.2017.11.033.
- 422 [38] Li, L., Khandelwal, K., 2015. Topology optimization of structures with length-scale effects using elasticity with  
423 microstructure theory. *Computers & Structures* 157, 165–177. doi:10.1016/j.compstruc.2015.05.026.
- 424 [39] Li, X., Liu, Q., Zhang, J., 2010. A micro–macro homogenization approach for discrete particle assembly–  
425 cosserat continuum modeling of granular materials. *International Journal of Solids and Structures* 47, 291–303.  
426 doi:10.1016/j.ijsolstr.2009.09.033.
- 427 [40] Liebenstein, S., Zaiser, M., 2018. Determining cosserat constants of 2D cellular solids from beam models. *Materials*  
428 *Theory* 2, 1–20. doi:10.1186/s41313-017-0009-x.
- 429 [41] Liu, S., Su, W., 2010. Topology optimization of couple-stress material structures. *Structural and Multidisciplinary*  
430 *Optimization* 40, 319–327. doi:10.1007/s00158-009-0367-3.
- 431 [42] Lu, Y., Wang, Y., 2022. Structural optimization of metamaterials based on periodic surface modeling. *Computer*  
432 *Methods in Applied Mechanics and Engineering* 395, 115057. doi:10.1016/j.cma.2022.115057.
- 433 [43] Mindlin, R.D., 1963. Microstructure in linear elasticity. Technical Report. Columbia Univ New York Dept of Civil  
434 Engineering and Engineering Mechanics. doi:10.1007/BF00248490.
- 435 [44] Mousanezhad, D., Babaei, S., Ebrahimi, H., Ghosh, R., Hamouda, A.S., Bertoldi, K., Vaziri, A., 2015. Hierarchical  
436 honeycomb auxetic metamaterials. *Scientific reports* 5, 1–8. doi:10.1038/srep18306.
- 437 [45] Otomori, M., Yamada, T., Izui, K., Nishiwaki, S., 2015. Matlab code for a level set-based topology optimiza-  
438 tion method using a reaction diffusion equation. *Structural and Multidisciplinary Optimization* 51, 1159–1172.  
439 doi:10.1007/s00158-014-1190-z.
- 440 [46] Park, H.C., Lakes, R.S., 1986. Cosserat micromechanics of human bone: strain redistribution by a hydration sensitive  
441 constituent. *Journal of biomechanics* 19, 385–397. doi:10.1016/0021-9290(86)90015-1.
- 442 [47] Peng, D., Merriman, B., Osher, S., Zhao, H., Kang, M., 1999. A pde-based fast local level set method. *Journal of*  
443 *computational physics* 155, 410–438. doi:10.1006/jcph.1999.6345.
- 444 [48] Pradel, F., Sab, K., 1998. Cosserat modelling of elastic periodic lattice structures. *Comptes Rendus de l’Académie*  
445 *des Sciences-Series IIB–Mechanics–Physics–Astronomy* 326, 699–704. doi:10.1016/S1251-8069(98)80002-X.
- 446 [49] Reis, F.D., Ganghoffer, J.F., 2012. Construction of micropolar continua from the asymptotic homogenization of beam  
447 lattices. *Computers & Structures* 112, 354–363. doi:10.1016/j.compstruc.2012.08.006.
- 448 [50] Ritchie, R.O., 2011. The conflicts between strength and toughness. *Nature Materials* 10, 817–822.  
449 doi:10.1038/nmat3115.
- 450 [51] Rokoš, O., Ameen, M.M., Peerlings, R.H.J., Geers, M.G.D., 2019. Micromorphic computational homogenization for  
451 mechanical metamaterials with patterning fluctuation fields. *Journal of the Mechanics and Physics of Solids* 123,  
452 119–137. doi:10.1016/j.jmps.2018.08.019.
- 453 [52] Rovati, M., Veber, D., 2007. Optimal topologies for micropolar solids. *Structural and Multidisciplinary Optimization*  
454 33, 47–59. doi:10.1007/s00158-006-0031-0.
- 455 [53] Rueger, Z., Lakes, R.S., 2016. Experimental cosserat elasticity in open-cell polymer foam. *Philosophical Magazine*  
456 96, 93–111. doi:10.1080/14786435.2015.1125541.
- 457 [54] Sab, K., Pradel, F., 2009. Homogenisation of periodic cosserat media. *International journal of computer applications*  
458 *in technology* 34, 60. doi:10.1504/IJCAT.2009.022703.
- 459 [55] Sanders, E.D., Aguiló, M.A., Paulino, G.H., 2018. Multi-material continuum topology optimization with arbitrary  
460 volume and mass constraints. *Computer Methods in Applied Mechanics and Engineering* 340, 798–823.  
461 doi:10.1016/j.cma.2018.01.032.



- 462 [56] Sethian, J.A., 1996. Level set methods, evolving interfaces in geometry, fluid mechanics computer vision, and  
463 materials sciences, isbn-13: 978-0521572026. Cambridge Monographs on Applied and Computational Mathematics,  
464 3 .
- 465 [57] Sigmund, O., 1997. On the design of compliant mechanisms using topology optimization. *Journal of Structural*  
466 *Mechanics* 25, 493–524. doi:10.1080/08905459708945415.
- 467 [58] Sigmund, O., 2001. A 99 line topology optimization code written in matlab. *Structural and multidisciplinary*  
468 *optimization* 21, 120–127. doi:10.1007/s001580050176.
- 469 [59] Sokolowski, J., Zolesio, J.P., 1992. Introduction to shape optimization, in: *Introduction to Shape Optimization*.  
470 Springer, pp. 5–12. doi:10.1007/978-3-642-58106-9.
- 471 [60] Su, W., Liu, S., 2016. Topology design for maximization of fundamental frequency of couple-stress continuum.  
472 *Structural and Multidisciplinary Optimization* 53, 395–408. doi:10.1007/s00158-015-1316-y.
- 473 [61] Su, W., Liu, S., 2020. Size-dependent microstructure design for maximal fundamental frequencies of structures.  
474 *Structural and Multidisciplinary Optimization* 62, 543–557. doi:10.1007/s00158-020-02510-w.
- 475 [62] Toupin, R., 1962. Elastic materials with couple-stresses. *Archive for rational mechanics and analysis* 11, 385–414.  
476 doi:10.1007/BF00253945.
- 477 [63] Tozoni, D., Dumas, J., Jianh, Z., Panetta, J., Panozzo, D., Zorin, D., 2020. A low-parametric rhombic microstructure  
478 family for irregular lattices. *ACM Transactions on Graphics (TOG)* 39(4), 101. doi:10.1145/3386569.3392451.
- 479 [64] Veber, D., Taliercio, A., 2012. Topology optimization of three-dimensional non-centrosymmetric micropolar bodies.  
480 *Structural and Multidisciplinary Optimization* 45, 575–587. doi:10.1007/s00158-011-0707-y.
- 481 [65] Wang, L., Cai, Y., Liu, D., 2018. Multiscale reliability-based topology optimization methodology for truss-like  
482 microstructures with unknown-but-bounded uncertainties. *Computer Methods in Applied Mechanics and Engineering*  
483 339, 358–388. doi:10.1016/j.cma.2018.05.003.
- 484 [66] Watts, S., Arrighi, W., Kudo, J., Tortorelli, D.A., White, D.A., 2019. Simple, accurate surrogate models of the elastic  
485 response of three-dimensional open truss micro-architectures with applications to multiscale topology design. *Struct*  
486 *Multidisc Optim* 60, 1887–1920. doi:10.1007/s00158-019-02297-5.
- 487 [67] Yamada, T., Izui, K., Nishiwaki, S., Takezawa, A., 2010. A topology optimization method based on the level set  
488 method incorporating a fictitious interface energy. *Computer Methods in Applied Mechanics and Engineering* 199,  
489 2876–2891. doi:10.1016/j.cma.2010.05.013.
- 490 [68] Yvonnet, J., Auffray, N., Monchiet, V., 2020. Computational second-order homogenization of materials with  
491 effective anisotropic strain-gradient behavior. *International Journal of Solids and Structures* 191-192, 434–448.  
492 doi:10.1016/j.ijsolstr.2020.01.006.
- 493 [69] Zhang, H.W., Wang, H., Chen, B.S., Xie, Z.Q., 2008. Analysis of Cosserat materials with Voronoi cell finite element  
494 method and parametric variational principle. *Computer methods in applied mechanics and engineering* 197, 741–755.  
495 doi:10.1016/j.cma.2007.09.003.
- 496 [70] Zhang, X.S., Paulino, G.H., Ramos Jr, A.S., 2018. Multimaterial topology optimization with multiple volume con-  
497 straints: Combining the zpr update with a ground-structure algorithm to select a single material per overlapping set.  
498 *International Journal for Numerical Methods in Engineering* 114, 1053–1073. doi:10.1002/nme.5736.
- 499 [71] Zheng, J., Luo, Z., Li, H., Jiang, C., 2018. Robust topology optimization for cellular composites with hybrid  
500 uncertainties. *International Journal for Numerical Methods in Engineering* 115, 695–713. doi:10.1002/nme.5821.
- 501 [72] Zheng, L., Kumar, S., Kochmann, D., 2021. Data-driven topology optimization of spinoid metamaterials  
502 with seamlessly tunable anisotropy. *Computer Methods in Applied Mechanics and Engineering* 383, 113894.  
503 doi:10.1016/j.cma.2021.113894.
- 504 [73] Zheng, X., Smith, W., Jackson, J., Moran, B., Cui, H., Chen, D., Ye, J., Fang, N., Rodriguez, N., Weisgraber, T.,  
505 Spadaccini, C.M., 2016. Multiscale metallic metamaterials. *Nature materials* 15, 1100–1106. doi:10.1038/nmat4694.